ISSN (Print) 1226 1750
ISSN (Online) 2233 6656
Journal of Magnetics 25(4), 463-468 (2020) https://doi.org/10.4283/JMAG.2020.25.4.463

Evaluation of Attenuation Correction Using Dixon based Bone Model for ^{18}F FDG Brain PET/MR: A Volunteer Study

Seok Hwan Yoon[1,2], Sang Rok Kim[1,3], and Hyung Jin Yang[1]*

[1]*Department of Biomedical Science, Korea University, 2511, Sejong Ro, Sejong City 30019, Republic of Korea*
[2]*Department of Nuclear Medicine, Seoul National University Hospital, 101, Daehak Ro, Jongno Gu, Seoul 03080, Republic of Korea*
[3]*Department of Radiation Safety Section, Korea institute of Radiological and Medical Sciences, 75, Nowon Ro, Nowon Gu, Seoul 01812, Republic of Korea*

(Received 31 August 2020, Received in final form 7 October 2020, Accepted 14 October 2020)

The present study aims to evaluate PET quantification for the fluoro deoxy glucose (FDG) brain PET images using two MR attenuation maps by comparing them with images using CT attenuation map in a healthy volunteer. The two MR attenuation maps include four segments of the Dixon sequence (soft tissue, fat, lung, and air), and five segmentations of the Dixon based bone model (soft tissue, fat, lung, air, and bone). Quantifications of the standardized uptake values (SUVs) for 133 regions of FDG brain PET images using voxel wise analyses revealed significant differences between CT and Dixon AC (mean difference = −0.93 ± 0.25). However, applying the Dixon based bone model AC reduced the estimation error compared with CTAC (mean difference = −0.66 ± 0.21). An attenuation map including bone information using the Dixon based bone model can reduce underestimation of SUV compared to Dixon from brain PET/MR imaging. In particular, errors were decreased more in the near skull regions than in central regions.

Keywords : Positron emission tomography (PET), Computed tomography (CT), Magnetic resonance image (MRI), Attenuation correction (AC), Dixon sequence, Dixon based bone model

1. Introduction

The integration of different imaging modes has been developed in recent years, including positron emission tomography (PET)/computed tomography (CT) and PET/magnetic resonance imaging (MRI), to enhance the diagnostic quality of examination in the field of molecular imaging [1]. A hybrid imaging scanner can co register anatomical and functional images and is therefore most appropriate for diagnosis. PET imaging involves the interaction of tissue with 511 keV photons emitted from the collision between a positron and an electron and their resulting annihilation. Compton scattering, leading to attenuation and scattering, can occur in this process. The photons undergoing Compton scattering deviate from their original path [2]. Thus, they may go undetected owing to attenuation or may be detected at the wrong location because of scattering. Photon attenuation and scattering corrections are essential to accurately quantify the radioactivity uptake [3]. Photon attenuation results in degradation in PET data acquisition and reconstruction. Thus, attenuation correction (AC) is generally performed using CT and MR based attenuation maps in PET/CT and PET/MR systems. In a combined PET/CT system, a CT image is used to generate an attenuation map for 511 keV photons [4]. The CT image is related to the electron density, and thus can be directly derived by scaling bone and soft tissue pixels with their respective scale factor calculated from the ratio of the mass attenuation coefficient at 511 keV for attenuation correction. Therefore, CT based attenuation correction (CTAC) is mostly used as standard for AC of PET data. However, in a simultaneous PET/MR system, MR signals are related to the proton density and longitudinal (T1) and transverse (T2) magnetization relaxation properties of the tissue under investigation, rather than the electron density. The most common method for deriving attenuation maps in a clinical PET/MR system is to classify MR images for segmentation of different tissue classes and assign appropriate linear attenuation coefficients (LACs) to each tissue class [5, 6].

©The Korean Magnetics Society. All rights reserved.
*Corresponding author: Tel: +82-44-860-1325
Fax: +82-44-860-1325, e mail: yangh@korea.ac.kr

© 2020 Journal of Magnetics

Standard Dixon sequence based tissue segmentation to separate water, fat, soft tissue, and air is incorporated into a dedicated PET/MR scanner. This is regarded as a routine protocol in clinical PET/MRI [7]. However, the brain is surrounded by cortical bone, which leads to quantification error because it is difficult to differentiate bone from soft tissue using the Dixon attenuation map, leading to bone being replaced by soft tissue in the map [8]. To obtain bone information and overcome the limitations of MR based attenuation maps, alternative methods have been proposed, including segmentation methods such as ultra short echo (UTE) and registration based methods using atlas templates [9-12]. Recently, the addition of a Dixon based bone model was used to assign bone information to the Siemens PET/MR system. This study aimed to evaluate the PET quantification between Dixon sequence and the superimposed model based bone compartment method for MR based attenuation correction (MRAC) compared with CTAC in fluoro deoxy glucose (FDG) PET brain imaging.

2. Methods

We tested a healthy volunteer using CT, Dixon sequence, and Dixon based bone model attenuation maps to evaluate the quantification of brain PET. The PET/CT and PET/MR images of a single consenting healthy adult volunteer (Gender: Male, Age: 36) were acquired following our clinical protocol.

2.1. PET/CT and PET/MR Acquisition

The PET emission scan of the volunteer used for the study was acquired from the PET/CT scanner, in order to eliminate the effect of the scanner between the PET/CT and PET/MR systems. PET/CT imaging was acquired in a single PET bed position after an injection of 185 MBq (5 mCi) of ^{18}F FDG. The volunteer's head was positioned in a head holder and attached to the patient bed. The PET emission data were acquired using a PET/CT scanner comprising a 40 slice CT detector (Biograph mCT40, Siemens Healthcare, Erlangen, Germany) in the sinogram mode for 10 min. A low dose CT, at 120 kVp, and 35 mAs, with 74 slices and 0.6 mm × 0.6 mm. 0.3 mm voxels, was also acquired. The CT images were reconstructed in a 512 × 512 × 112 matrix with voxel sizes of 0.59 mm × 0.59 mm × 3 mm for PET AC. For MR based attenuation maps, we acquired the vendor provided two point (water–fat) Dixon sequence (repetition time: 2300 ms; first echo time: 1.23 ms; second echo time: 2.46 ms; flip angle: 10° coronal orientation; voxel size: 2.6 mm × 2.6 mm × 3.12 mm) using a PET/MRI scanner (Biograph mMR 3.0T Siemens Healthcare, Erlangen, Germany).

2.2. CT and MR based attenuation map

We performed the CT based attenuation map as the gold standard and compared it with the two MR based attenuation maps, namely the Dixon sequence and Dixon based bone model methods. CT data can directly convert linear attenuation coefficients (LACs) by photon attenuation. CT attenuation maps have therefore been the most widely used technique on PET images for attenuation correction.

2.2.1. CT μ map

The CT based attenuation map is scaled by a bi linear function on low dose CT data to represent the LACs at 511 keV.

2.2.2. Dixon μ map

Dixon imaging was performed with a two point sequence (water–fat). The manufacturer provides four segmentations for air (LAC: 0.0 cm^{-1}), fat (LAC: 0.0854 cm^{-1}), lung (LAC: 0.0224 cm^{-1}) and soft tissue (LAC: 0.1 cm^{-1}). In this method, the bone tissue LAC was replaced by soft tissue.

2.2.3. Dixon based bone model μ map

This method generates an attenuation map based on the Dixon sequence based attenuation map. Bone information is added to the Dixon attenuation map using the model based bone segmentation algorithm (Syngo MR E11P; Siemens AG Healthcare) that applies continuous LAC at 511 keV for bone segmentation. Five segmentations with bone information can be assigned from an integrated bone atlas by registration of MR images of the subject to the MR image of the atlas template. The atlas contains sets of pre aligned MR image and bone mask pairs with bone densities as LACs (cm^{-1}) at a PET energy of 511 keV [13]. The continuous LACs of bone segmentation is assigned as being greater than 0.1 cm^{-1} representing value above soft tissue in this study (0.11-0.13 cm^{-1}).

2.3. Image Reconstruction and Analysis

PET data were reconstructed from the emission data of the PET/CT using CT and two MR based attenuation maps. The reconstruction was performed using the offline reconstruction software Siemens e7 tools. The MR based attenuation maps were registered and resliced to the standard CT attenuation map using statistical parametric mapping (SPM8; University College London). The recon struction process applied the Ordinary Poisson Ordered Subset Expectation Maximization (OP OSEM) algorithm with 3 iterations and 21 subsets. PET images were smooth

ed by applying a three dimensional Gaussian post smooth ing filter of 3 mm in full width at half maximum. After reconstruction, all PET data were spatially normalized to the Scenium software (Syngo.via platform, version VB10B, Neurology analysis; Siemens Healthcare) to evaluate the spatial error of PET intensity with different modality attenuation maps.

We performed voxel wise analyses using Scenium. The standardized uptake value (SUV) was measured in 11 brain regions to compare the percentage difference, and we performed Bland–Altman analyses to find intersystem variability in 133 brain regions between the CT and two MR based attenuation maps. We calculated the relative mean SUV of each brain region and its ratio to the whole brain (SUVr) to assess potential regional differences. The percentage difference was calculated in each brain region and was defined as

$$\text{Relative difference (\%)} = \frac{\text{PET}_{\text{MRAC}} - \text{PET}_{\text{CTAC}}}{\text{PET}_{\text{CTAC}}} \times 100\,,$$

where, PET_{MRAC} and PET_{CTAC} are the average SUV measured in a brain region using MR and CT based maps, respectively. Statistical analyses were performed using SPSS software (version 23; SPSS, IBM, Chicago, IL, USA).

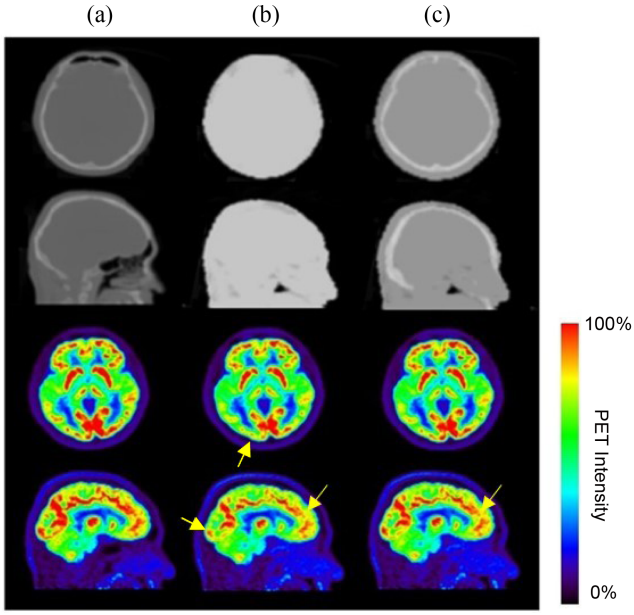

Fig. 1. (Color online) Attenuation maps and reconstructed PET images corrected using attenuation maps CTAC (a), MRAC-Dixon (b), MRAC-Dixon-based bone model (c). CT and MR based attenuation maps are presented in the first row (transverse view) and second row (sagittal view). Reconstructed PET images are shown in the third row (transverse view) and fourth row (sagittal view). Arrows (yellow) indicate underestimation of PET intensity for MRAC compared with CTAC

3. Results

The results of CTAC, MRAC using Dixon sequence, and MRAC using Dixon based bone model method applied to the identical emission data acquired using the PET/CT scanner are shown in Fig. 1. The two MR based attenuation maps showed errors in the air cavities of the sinuses compared with the CT attenuation map. The PET intensity with the two MR based attenuation maps show ed underestimation compared to the standard CT attenuation map, and the Dixon based bone model method reduced the SUV estimation error present in the Dixon

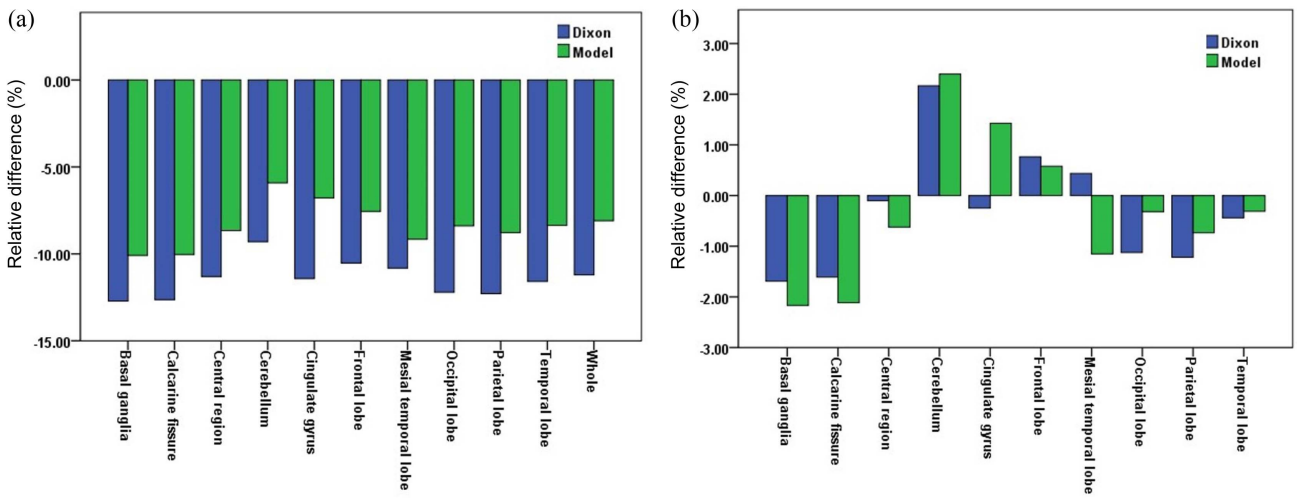

Fig. 2. (Color online) Percentage difference of SUV (a) and SUVr (b) between CT and MR based attenuation maps (Dixon and Dixon based bone model) in ^{18}F-FDG brain PET.

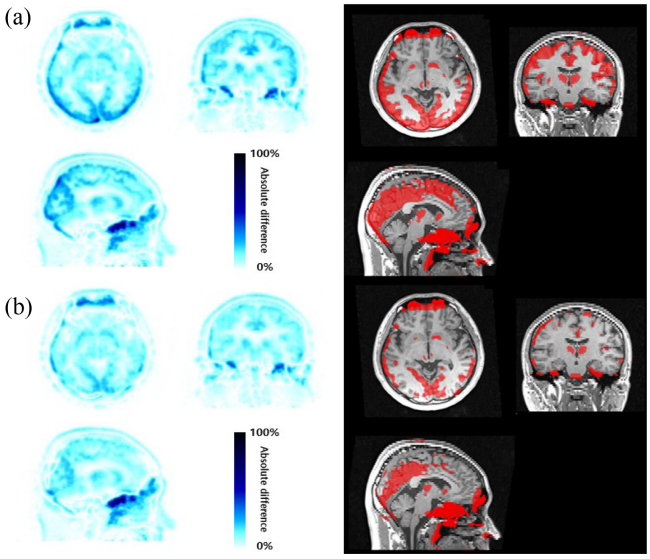

Fig. 3. (Color online) Difference of intensity in FDG PET images (left) and overlaid with MR images (right). MRAC-Dixon in comparison to CTAC (a). MRAC-Dixon-based bone model in comparison to CTAC (b). Red color shows the differences between CTAC and MRAC.

method.

The percentage difference in SUV and SUVr for the 11 brain regions are presented in Fig. 2. The difference in the SUV of the brain regions using an MR based attenuation map was underestimated compared with the CT attenuation map. The percentage difference magnitudes of the SUV from CTAC were greater than 11 % for the Dixon AC and 8 % for the Dixon based bone model AC. The Dixon based bone model AC and SUV improved the under-

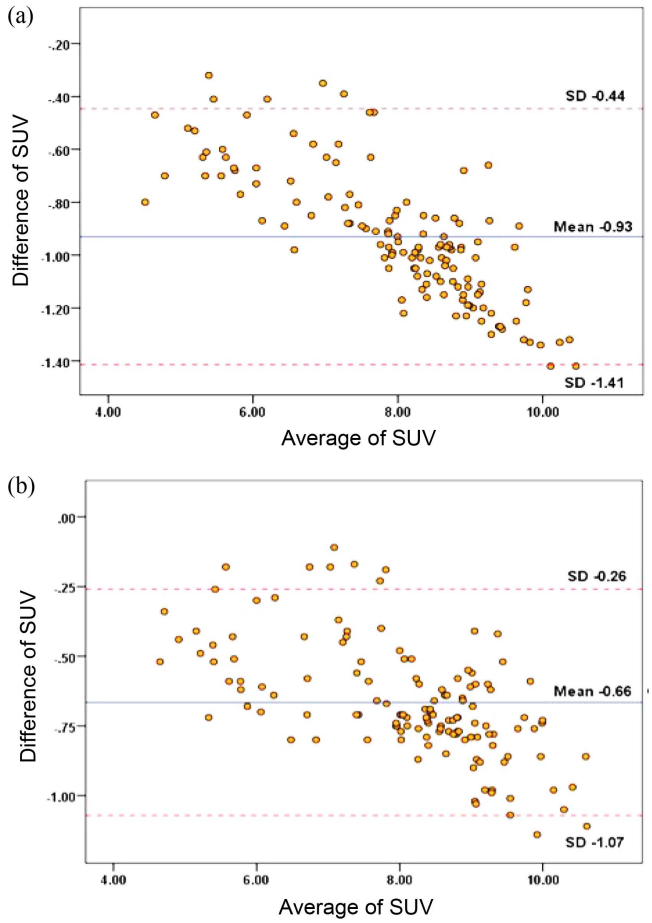

Fig. 4. (Color online) The Bland–Altman plots of voxel by voxel for mean SUV in 133 regions of brain between CTAC and MRAC. SUV with CT and MR-Dixon (a), SUV with CT and MR- Dixon-based bone model (b).

Table 1. The percent difference of SUV and SUVr for MR based attenuation maps without and with bone information (Dixon and Dixon based bone model) compared with CT based attenuation map in 11 brain regions of a volunteer. The SUVr was calculated as ratio of each regions and whole brain.

Brain region	% diff. SUV		% diff. SUVr	
	Dixon (without bone)	Model (with bone)	Dixon (without bone)	Model (with bone)
Basal ganglia	–12.71	–10.09	–1.69	–2.17
Calcarine fissure	–12.20	–8.39	–1.61	–2.11
Central region	–11.30	–8.66	–0.11	–0.62
Cerebellum	–9.30	–5.91	2.15	2.37
Cingulate gyrus	–11.42	–6.77	–0.24	1.44
Frontal lobe	–10.53	–.7.56	0.76	0.58
Mesial temporal lobe	–10.82	–9.16	0.43	–1.16
Occipital lobe	–12.20	–8.39	–1.12	–0.32
Parietal lobe	–12.29	–8.77	–1.22	–0.74
Temporal lobe	–11.59	–8.37	–0.43	–0.30
Whole brain	–11.20	–8.09	-	-

estimation of all brain regions compared with the Dixon sequence. However, the central brain region such as basal ganglia and cingulate gyrus had a higher difference than cortical structures such as the frontal, parietal and temporal lobes, based on a comparison of SUVr.

Figure 3 shows the spatial error of PET intensity between CTAC and the two MRAC. There were remarkable differences in almost all brain regions. Both MRAC methods had significant errors of attenuation maps in the air cavities of the sinuses because of mis segmentation. However, for the Dixon based bone model, there was a reduced error, in particular of cortical structures such as the frontal, parietal, and temporal lobes, compared to the standard Dixon sequence.

Figure 4 shows the results of the Bland–Altman plots, where the mean difference in the horizontal direction indicates the estimated error. The mean difference was -0.93 ± 0.25 for Dixon and -0.66 ± 0.21 for the Dixon based bone model. This implies that the underestimation in mean SUV was improved when PET images were obtained using the Dixon based bone model for attenuation correction.

4. Discussion

In this study, we investigated FDG brain PET images using CT and two MR based attenuation maps, namely the Dixon sequence and Dixon based bone model, in case of a healthy volunteer. The Dixon based bone model method is added to bone segmentation in the standard Dixon attenuation map to overcome problems with accuracy of bone information in the PET/MR system. The results demonstrated that voxel wise analyses in all brain regions revealed underestimation in the two MR based attenuation maps compared with CTAC ($p < 0.05$) (Fig. 2). When reconstructed PET images included bone information from the Dixon based bone model AC, the SUV increased in all brain regions compared with the standard Dixon from both the percentage difference result and the mean difference of Bland–Altman analyses (Fig. 2, Fig. 4). The difference in intensity from PET images using the Dixon attenuation map without bone information resulted in significant errors near skull regions such as the frontal, parietal, and temporal lobes compared with CTAC (Fig. 3), because photons from the edge of the brain travel longer average path lengths through the skull than photons from the center [14]. We also observed that Dixon including bone information, showed smaller errors in the near skull regions than in the center regions (Fig. 2, Fig. 3). However, the central regions of the brain had higher errors in Dixon with bone than in Dixon without bone, from the SUVr comparison. Normalization of PET intensity by reference value can reduce systemic error; however, it can inflate regional values, particularly in cases where group differences actually exist between the reference values [15]. In our study, scaling PET images by whole brain resulted in regional over and underestimations. These regional trends matched results from previous studies [16, 17]. These results could explain why adding bone information improves errors near the skull regions and reduces underestimation in all regions of the brain.

In addition, there are limitations to this study. First, the two MR based attenuation maps resulted in errors in the air cavities of the sinuses compared with the CT attenuation map (Fig. 1). Most segmented and atlas based MR derived attenuation maps can cause misclassification errors in soft tissue, bone, and air that interface in the areas around the sinuses [17]. Large errors are likely to be induced in the attenuation corrected PET images, and the accuracy of the Dixon-based bone model may be affected by the individual subject's skull or brain anatomy. This especially relates to the frontal lobe thickness, which is highly variable, and can cause artefacts by mis-registration between the Dixon images and the bone template [18]. Second, this study used a healthy volunteer instead of a phantom to segment tissues such as soft tissues and bone. However, the aim of this study was to compare attenuation correction between without bone and with bone information, rather than exact diagnosis. We believe that the results of this study can be used as base data for patient studies. The most widely used clinical PET/MRI system from Siemens offers the UTE sequence along with the Dixon sequence for attenuation correction in brain PET/MR imaging. The UTE sequence can be used to distinguish cortical bone by short relaxation time. However, previous studies [16, 19, 20] demonstrated that UTE-based AC had errors in determining the boundary between soft tissue and air and suffered from five times longer imaging time than Dixon [16]. Thus, we think that further studies should be performed between UTE and Dixon based bone model by attenuation correction with bone information for large number of patients in PET/MR system. In this study, we aimed to obtain more accurate quantification and segmentation using the Dixon-based bone model method compared with Dixon; however, it is necessary for further studies to address mis-registration by error and limited atlas-template.

5. Conclusion

This study evaluated the attenuation correction of MR-

based attenuation maps using standard Dixon and Dixon-based bone model methods by comparing their images with those using CT AC as gold standard in ^{18}F-FDG brain PET/MR imaging. All brain regions underestimated the SUV in both models of MRAC compared to CTAC. An attenuation map including bone information using the Dixon-based bone model can decrease the underestimation of SUV in all regions of the brain. In particular, errors were decreased more in the near skull regions than in the central regions compared to standard Dixon from brain PET/MR imaging. The Dixon-based bone model is more useful for improving the quantitative accuracy than the standard Dixon.

Acknowledgments

This study was supported by the Research Foundation of Korea University and was approved by the Institutional Review Board of Korea University.

References

[1] A. Kjaer, Cancer Imaging **14** (2014).
[2] P. Zanzonico, Semin. Nucl. Med. **34**, 2 (2004).
[3] Ninon Burgos, Kris Thielemans, M. Jorge Cardoso, Pawel Markiewicz, Jieqing Jiao, John Dickson, John S. Duncan, David Atkinson, Simon R. Arridge, Brian F. Hutton, and Sébastien Ourselin, IEEE Nuclear Science Symposium and Medical Imaging Conference (NSS/MIC) (2014).
[4] M. E. Lindemann, F. Nensa, and H. H. Quick, PLoS ONE **14** (2019).
[5] A. Martinez-Moller, M. Souvatzoglou, G. Delso, R. A. Bundschuh, C. Chefd'hotel, S. I. Ziegler, N. Navab, M. Schwaiger, and S. G. Nekolla, J. Nucl. Med. **50**, 4 (2009).
[6] S. H. Keller, S. Holm, A. E. Hansen, B. Sattler, F. Andersen, T. L. Klausen, L. Højgaard, A. Kjær, and T. Beyer, Magn. Reson. Mater. Phy. **26**, 1 (2013).
[7] I. Bezrukov, F. Mantlik, H. Schmidt, B. Schölkopf, and B. J. Pichler, Semin. Nucl. Med. **43**, 1 (2013).
[8] D. H. Paulus, H. H. Quick, C. Geppert, M. Fenchel, Y. Zhan, G. Hermosillo, D. Faul, F. Boada, K. P. Friedman, and T. Koesters, J. Nucl. Med. **56**, 7 (2015).
[9] W. T. Dixon, Radiology **153** (1984).
[10] C. Catana, A. Drzezga, W. D. Heiss, and B. R. Rosen, J. Nucl. Med. **53**, 12 (2012).
[11] T. Beyer, M. Weigert, H. H. Quick, U. Pietrzyk, F. Vogt, C. Palm, G. Antoch, S. P. Müller, and A. Bockisch, Eur. J. Nucl. Med. Mol. Imaging **35**, 6 (2008).
[12] H. R. Marshall, J. Patrick, D. Laidley, F. S. Prato, J. Butler, J. Théberge, R. T. Thompson, and R. Z. Stodilka, Med. Phys. **40**, 8 (2013).
[13] T. Koesters, K. P. Friedman, M. Fenchel, Y. Zhan, G. Hermosillo, J. Babb, I. O. Jelescu, D. Faul, F. E. Boada, and T. M. Shepherd, J. Nucl. Med. **57**, 6 (2016).
[14] F. L. Andersen, C. N. Ladefoged, T. Beyer, S. H. Keller, A. E. Hansten, L. Høgild, A. Kjær, I. Law, and S. Holm, Neuroimage **84** (2014).
[15] P. Borghammer, K. Y. Jonsdottir, P. Cumming, K. Ostergaard, K. Vang, M. Ashkanian, M. Vafaee, P. Iversen, and A. Gjedde, NeuroImage **40**, 2 (2008).
[16] J. C. Dickson, C. O'Meara, and A. Barnes, Eur. J. Nucl. Med. Mol. Imaging **41**, 6 (2014).
[17] U. C. Anazodo, J. D. Thiessen, T. Ssali, J. Mandel, M. Günther, J. Butler, W. Pavlosky, F. S. Prato, R. T. Thompson, and K. S. Lawrence, Front. Neurosci. **8** (2014).
[18] V. Keereman, Y. Fierens, T. Broux, Y. D. Deene, M. Lonneux, and S. Vandenberghe, J. Nucl. Med. **51**, 5 (2010).
[19] V. Keereman, P. Mollet, Y. Berker, V. Schulz, and S. Vandenberghe, MAGMA **26**, 1 (2013).
[20] A. P. Aitken, D. Giese, C. Tsoumpas, P. Schleyer, S. Kozerke, C. Prieto, and T. Schaeffter, Med. Phys. **41**, 1 (2014).